

2D-FFTLog: Efficient computation of real space covariance matrices for galaxy clustering and weak lensing

Xiao Fang (方啸),¹* Tim Eifler,¹ and Elisabeth Krause^{1,2}

¹Department of Astronomy and Steward Observatory, University of Arizona, 933 N Cherry Ave, Tucson, AZ 85719, USA

²Department of Physics, University of Arizona, 1118 E. Fourth Street, Tucson, AZ 85721, USA

Accepted XXX. Received YYY; in original form ZZZ

ABSTRACT

Accurate covariance matrices for two-point functions are critical for inferring cosmological parameters in likelihood analyses of large-scale structure surveys. Among various approaches to obtaining the covariance, analytic computation is much faster and less noisy than estimation from data or simulations. However, the transform of covariances from Fourier space to real space involves integrals with two Bessel integrals, which are numerically slow and easily affected by numerical uncertainties. Inaccurate covariances may lead to significant errors in the inference of the cosmological parameters. In this paper, we introduce a 2D-FFTLog algorithm for efficient, accurate and numerically stable computation of non-Gaussian real space covariances. The 2D-FFTLog algorithm is easily extended to perform real space bin-averaging. We apply the algorithm to the covariances for galaxy clustering and weak lensing for a DES Y3-like and an LSST Y1-like survey, and demonstrate that for both surveys, our algorithm can produce numerically stable angular bin-averaged covariances at the flat sky limit, which are sufficiently accurate for inferring cosmological parameters.

Key words: cosmology: theory – large-scale structure of Universe – dark energy – cosmological parameters

1 INTRODUCTION

Ongoing and upcoming photometric and spectroscopic surveys, such as KiDS¹, HSC², DES³, LSST⁴, WFIRST⁵, SPHEREx⁶, eBOSS⁷, DESI⁸, Subaru PFS⁹, Euclid¹⁰, aim for precise measurements of cosmological parameters. While likelihood-free approaches are emerging as a tool for cosmological inference (e.g., Akeret et al. 2015; Peel et al. 2017), most of cosmological analyses still rely on a likelihood function $\mathcal{L}(\mathbf{D}|\mathbf{M})$, and the simplest and most common choice is

a multivariate Gaussian distribution,

$$\mathcal{L}(\mathbf{D}|\mathbf{M}(\mathbf{p})) = \frac{1}{\sqrt{(2\pi)^{N_D} |\mathbf{C}|}} \exp \left\{ -\frac{1}{2} [\mathbf{M}(\mathbf{p}) - \mathbf{D}]^T \mathbf{C}^{-1} [\mathbf{M}(\mathbf{p}) - \mathbf{D}] \right\}, \quad (1)$$

where \mathbf{D} is the data vector, $\mathbf{M}(\mathbf{p})$ is the model prediction with parameters \mathbf{p} , \mathbf{C} is the covariance matrix, and N_D is the dimension of the data vector. Limitations of the Gaussian likelihood assumption are discussed in e.g., Hartlap et al. (2009); Sato et al. (2010). However, its impact on the cosmological parameter inferences may be insignificant for future surveys (e.g., Lin et al. 2019). We will only consider data vectors consisting of two-point correlation functions in real space, since many weak lensing analyses are performed in real space, such as KiDS (Hildebrandt et al. 2017), DES (Troxel et al. 2018; Abbott et al. 2018), and HSC (Hamana et al. 2019).

Broadly, there are three approaches to obtaining covariance matrices: estimation from simulations, estimation from data, and analytical computation. Estimation from simulations requires a large number of large, high resolution numerical simulations, due to the intrinsic noise properties of the maximum likelihood estimator of the covariance Taylor et al. (2013); Dodelson & Schneider (2013); Taylor & Joachimi (2014). This approach is computationally too expensive as

* E-mail: xfang@email.arizona.edu

¹ Kilo-Degree Survey, <http://kids.strw.leidenuniv.nl/>

² Hyper Suprime-Cam, <https://www.naoj.org/Projects/HSC/>

³ Dark Energy Survey, <https://www.darkenergysurvey.org>

⁴ Large Synoptic Survey Telescope, <https://www.lsst.org/>

⁵ Wide Field Infrared Survey Telescope, <https://wfirst.gsfc.nasa.gov/>

⁶ Spectro-Photometer for the History of the Universe, Epoch of Reionization, and Ices Explorer, <http://spherex.caltech.edu/>

⁷ Extended Baryon Oscillation Spectroscopic Survey, <https://www.sdss.org/surveys/eboss/>

⁸ Dark Energy Spectroscopic Instrument, <https://www.desi.lbl.gov/>

⁹ Subaru Prime Focus Spectrograph, <https://pfs.ipmu.jp/>

¹⁰ <https://www.euclid-ec.org/>

the number of data points increases (but see [Joachimi 2017](#); [Friedrich & Eifler 2018](#), for hybrid estimators). Estimation from data has the advantage of not depending on the model used in the simulations or in the analytic calculation. However, the estimated covariance is noisy due to the limited number of independent realizations available from the data, leading to the loss of information ([Hartlap et al. 2007](#); [Dodelson & Schneider 2013](#); [Sellentin & Heavens 2017](#)). Moreover, because the unbiased covariance estimator of simulations or data leads to biased estimation of the precision matrix, an additional term must be introduced to the likelihood to be marginalized over in order to correct the impact on parameter inferences ([Sellentin & Heavens 2016](#)). Altogether, there is a strong motivation for robust, precise methods for analytic covariances. We focus on the efficient and accurate evaluation of real space covariance matrices, assuming that a sufficiently accurate model of the Fourier space covariance exists.

The transform of a covariance matrix of 3D statistics from Fourier space to real space involves double integrals with two spherical Bessel functions in the integrand (i.e., “double Bessel integrals”). It is numerically challenging due to the highly oscillatory nature of the spherical Bessel functions. For projected angular statistics, the transform involves double summations over multipole moments weighted by combinations of Legendre and associated Legendre polynomials. Assuming narrow angles or flat sky, the transform is well approximated by double integrals with two Bessel functions in the integrand, and suffers from similar numerical challenges. We will call the former “curved sky covariance” and the latter “flat sky covariance”.

In this paper, we present a new FFTLog based algorithm to efficiently compute the double Bessel integrals for the real space covariance matrices. In §2, we introduce the 2D-FFTLog algorithm for covariances and detail its implementation. The 2D-FFTLog avoids the computation of hypergeometric functions, leading to simpler expressions. It is worth noting that our method, when only considering the Gaussian covariances, is similar in nature to the method proposed in §3 of [Li et al. \(2019\)](#).

Furthermore, covariance matrices are often averaged over each real space (or angular) bin since the correlation functions are measured in bins (e.g., [Singh et al. 2017](#)). We present an accurate way of bin-averaging in our 2D-FFTLog algorithm. In §3, we apply our algorithm to analytic covariance matrices for the joint-probe analysis of galaxy clustering, galaxy-galaxy lensing (GGL), and cosmic shear. In §4, we compare the flat sky FFT covariances to the flat sky brute-force (BF) covariances from the traditional quadrature integration and the curved sky covariances in the context of future surveys such as DES Year 3 (DES Y3) and LSST Year 1 (LSST Y1). We also perform simulated likelihood analyses and show that the flat sky covariances from the 2D-FFTLog algorithm do not introduce biases in the cosmological parameters for these surveys. Finally, we discuss other applications and summarize in §5.

We emphasize that the method presented in this paper can be directly applied to future surveys including DES, LSST, and WFIRST. Its advantage in efficiency will be even more prominent when more tomographic bins are used, and when more probes (such as CMB lensing, cluster clustering and cluster lensing) are jointly analyzed.

2 2D-FFTLOG FOR COVARIANCES

For covariances of 3D statistics, the numerically challenging transform takes the form of double Bessel integrals

$$C(r_1, r_2) = \int_0^\infty \frac{dk_1}{k_1} \int_0^\infty \frac{dk_2}{k_2} f(k_1, k_2) j_{\ell_1}(k_1 r_1) j_{\ell_2}(k_2 r_2), \quad (2)$$

while the Gaussian covariances take the form of

$$C_G(r_1, r_2) = \int_0^\infty \frac{dk}{k} f(k) j_{\ell_1}(k r_1) j_{\ell_2}(k r_2). \quad (3)$$

The functions $f(k)$ and $f(k_1, k_2)$ are smooth functions of k or k_1, k_2 . To evaluate all the elements of an $N \times N$ covariance matrix, the brute-force quadrature integration of Eq. (3) will take order of $N^2 N_k$ steps, where N_k is the number of k points sampled, while Eq. (2) will take order of $N^2 N_k^2$ steps. Furthermore, the rapidly oscillatory Bessel functions, possibly beating with each other, require very small sampling space, especially when r_1, r_2 are large.

For flat sky covariances of projected statistics, the spherical Bessel functions j_ℓ 's are replaced by Bessel functions, which can be converted back to this form using $J_n(z) = \sqrt{2z/\pi} j_{n-1/2}(z)$ (see §3 for relevant discussions). The curved sky covariances are detail in §4.1.4.

The FFTLog algorithm ([Hamilton 2000](#)) has been used to efficiently perform single Bessel integrals, i.e., the Hankel transforms, in the form of $\int_0^\infty dk f(k) j_\ell(kr)$ or $\int_0^\infty dk f(k) J_n(kr)$, with logarithmically sampled k . The core idea of the FFTLog algorithm involves a power-law decomposition of $f(k)$, so that each term in the decomposition can be integrated analytically. The FFTLog has found many applications in cosmology, including the one-loop order ([Schmittfull et al. 2016](#); [McEwen et al. 2016](#); [Fang et al. 2017](#)) and two-loop order nonlinear perturbation theories ([Schmittfull & Vlah 2016](#); [Simonović et al. 2018](#); [Slepian 2018](#)), the angular power spectra, bispectra ([Assassi et al. 2017](#); [Grasshorn Gebhardt & Jeong 2018](#); [Schöneberg et al. 2018](#); [Fang et al. 2019](#); [Slepian et al. 2019](#)) and trispectra ([Lee & Dvorkin 2020](#)), the real space Gaussian covariances ([Slepian et al. 2019](#)), and the Fourier space non-Gaussian covariances ([Lee & Dvorkin 2020](#)).

In particular, the angular power spectra and bispectra without the Limber approximation contain double Bessel integrals in the form of Eq. (3). The same power-law decomposition leads to double Bessel transforms of power laws, which have analytical solutions containing Gauss hypergeometric functions (as shown in [Assassi et al. 2017](#); [Grasshorn Gebhardt & Jeong 2018](#); [Schöneberg et al. 2018](#)). We refer to this method as the 1D-FFTLog method. Note that the 1D-FFTLog method cannot be applied to the non-Gaussian covariances Eq. (2). Hypergeometric functions can be numerically challenging to evaluate, and require specialized methods to improve the speed and stability ([Assassi et al. 2017](#); [Grasshorn Gebhardt & Jeong 2018](#); [Schöneberg et al. 2018](#)). [Fang et al. \(2019\)](#) presents a new method for efficiently computing non-Limber angular power spectra with a generalized FFTLog algorithm without invoking hypergeometric functions, but it is not applicable to covariances.

[Slepian et al. \(2019\)](#) introduces a “rotation method”, which decomposes the spherical Bessel functions into series of products of polynomials and sine/cosine functions, and computes them with the FFTLog algorithm. This method is especially useful for computing Gaussian covariances of

3D statistics and possibly the non-Limber angular power spectra, at least at low ℓ 's. However, it may not be applied to non-Gaussian covariances, as well as covariances of projected statistics involving J_n 's which cannot be written in terms of sine/cosine functions.

The 2D-FFTLog algorithm presented here is a generalization of the original FFTLog. In §2.1, we introduce the algorithm for the general non-Gaussian covariance integral Eq. (2). We also show in §2.1.1 that the Gaussian covariance integral Eq. (3) can be evaluated with the same algorithm. In §2.2 we present a simple way to perform real space bin-averaging.

2.1 Transform for Non-Gaussian Covariances

We decompose the two-variable smooth function $f(k_1, k_2)$ in Eq. (2) into a series of products of two power-laws, i.e., 2-dimensional Fourier series in the $\log k_1$ - $\log k_2$ space, and assume the k_1, k_2 arrays are sampled logarithmically and are identical in binning (shorthand as k and using its subscript to denote the element index),

$$f(k_p, k_q) = \frac{1}{N^2} \sum_{m=-N/2}^{N/2} \sum_{n=-N/2}^{N/2} \tilde{c}_{mn} k_0^{-i\eta_m} k_0^{-i\eta_n} k_p^{\nu_1+i\eta_m} k_q^{\nu_2+i\eta_n}$$

$$\rightarrow \text{and } c_{mn} = W_m W_n \tilde{c}_{mn}$$

$$= W_m W_n \sum_{p=0}^{N-1} \sum_{q=0}^{N-1} \frac{f(k_p, k_q)}{k_p^{\nu_1} k_q^{\nu_2}} e^{-2\pi i(m p + n q)/N}, \quad (4)$$

where N is the size of the k array. $\eta_m = 2\pi m/(N\Delta_{\ln k})$, ν_1, ν_2 are the real parts of the power law indices (which we call ‘‘bias parameters’’), and $\Delta_{\ln k}$ is the linear spacing in $\ln k$, e.g., $k_q = k_0 \exp(q\Delta_{\ln k})$ with k_0 being the smallest value in the k_1 array. For a real function $f(k_1, k_2)$, the Fourier coefficients obey $\tilde{c}_{mn}^* = \tilde{c}_{-m, -n}$. c_{mn} are the filtered Fourier coefficients, which are smoothed along both axes at large m, n by the one-dimensional window function \mathbf{W} .¹¹ W_m, W_n are the m -th and n -th elements of \mathbf{W} . We then use the smoothed coefficients c_{mn} for the remaining computation.

With the double-power-law decomposition, Eq. (2) becomes

$$C(r_1, r_2) = \frac{1}{N^2} \sum_{m, n=-N/2}^{N/2} c_{mn} k_0^{-i(\eta_m + \eta_n)}$$

$$\int_0^\infty \frac{dk_1}{k_1} \int_0^\infty \frac{dk_2}{k_2} k_1^{\nu_1+i\eta_m} k_2^{\nu_2+i\eta_n} j_{\ell_1}(k_1 r_1) j_{\ell_2}(k_2 r_2)$$

$$= \frac{1}{N^2} \sum_{m, n=-N/2}^{N/2} c_{mn} k_0^{-i(\eta_m + \eta_n)}$$

$$\int_0^\infty \frac{dk_1}{k_1} k_1^{\nu_1+i\eta_m} j_{\ell_1}(k_1 r_1) \int_0^\infty \frac{dk_2}{k_2} k_2^{\nu_2+i\eta_n} j_{\ell_2}(k_2 r_2)$$

$$= \frac{\pi}{16r_1^{\nu_1} r_2^{\nu_2}} \frac{1}{N^2} \sum_{m, n=-N/2}^{N/2} c_{mn} k_0^{-i(\eta_m + \eta_n)} r_1^{-i\eta_m} r_2^{-i\eta_n}$$

$$\times g_{\ell_1}(\nu_1 + i\eta_m) g_{\ell_2}(\nu_2 + i\eta_n), \quad (5)$$

¹¹ We use the 1D window function \mathbf{W} described in Appendix C of McEwen et al. (2016).

where in the third equality we use a formula of Bessel functions (Eq. 11.4.16 of Abramowitz & Stegun 1972), an identity of Bessel functions) and define function $g_\ell(z)$ as

$$g_\ell(z) = 2^z \frac{\Gamma\left(\frac{\ell+z}{2}\right)}{\Gamma\left(\frac{3+\ell-z}{2}\right)}, \quad -\ell < \Re(z) < 2. \quad (6)$$

The valid ranges of ‘‘bias parameters’’ ν_1, ν_2 are thus $-\ell_1 < \nu_1 < 2$ and $-\ell_2 < \nu_2 < 2$, within which the bias parameters can be chosen arbitrarily, although different values can cause different levels of ringing effects at edges. In addition, integer values of ν_1, ν_2 should be avoided to avoid hitting singularities of the Gamma function. For convenience, we set $\nu_1 = \nu_2 = 1.01$. In contrast to 1D-FFTLog algorithms, the 2D-FFTLog does not need Gauss hypergeometric functions.

In principle, the r_1, r_2 arrays are independent of the k array. However, to take full advantage of the FFTLog algorithm and simplify the calculation, we assume that r_1, r_2 are identical arrays (shorthand as r array), logarithmically sampled with linear spacing $\Delta_{\ln r}$ in $\ln r$, and set $\Delta_{\ln r} = \Delta_{\ln k}$. Therefore, the last summation in Eq. (5) can be written as

$$C(r_p, r_q) = \frac{\pi}{16r_p^{\nu_1} r_q^{\nu_2}} \text{IFFT2}[c_{mn}^*(k_0 r_0)^{i(\eta_m + \eta_n)} \times g_{\ell_1}(\nu_1 - i\eta_m) g_{\ell_2}(\nu_2 - i\eta_n)], \quad (7)$$

where r_p, r_q ($p, q = 0, 1, \dots, N-1$) are the p -th and q -th elements in the r array, respectively. IFFT2 stands for the two-dimensional Inverse Fast Fourier Transform.

The 2D-FFTLog method uses 2D FFT twice. Thus, it is an $\mathcal{O}(N^2 \log N)$ algorithm. Note that by performing the inverse FFT, we obtain an $N \times N$ real space covariance matrix for the N logarithmically sampled r values. In practice, such a fine-grid matrix of step size $\Delta_{\ln r}$ is not needed, and one may choose to calculate the desired smaller-size covariance directly from the c_{mn} matrix without using the inverse FFT, i.e., directly summing over m, n in the last line of Eq. (5) for each covariance element. Whether the latter option is more optimal depends on the size of the desired matrix. In practice, bin-averaging is performed on covariance matrices, which acts as smoothing and needs less sampling points, hence computation time, for a given accuracy requirement. We discuss our bin-averaging algorithm in §2.2.

2.1.1 Special Case: Gaussian Covariance Integrals

The Gaussian covariance C_G can be considered as a special case of the non-Gaussian covariance when $f(k_1, k_2)$ contains a Dirac delta function $\delta_D(k_1 - k_2)$, which makes the separation of k_1 and k_2 difficult. However, in the quadrature integration, the integral is discretized, the Dirac delta is converted to the Kronecker delta, making the separation trivial.

Writing C_G (Eq. 3) in a discrete sum

$$C_G = \lim_{\Delta_{\ln k} \rightarrow 0} \Delta_{\ln k} \sum_p f(k_p) j_{\ell_1}(k_p r_1) j_{\ell_2}(k_p r_2)$$

$$= \lim_{\Delta_{\ln k} \rightarrow 0} \Delta_{\ln k} \sum_p \sum_q f(k_p) j_{\ell_1}(k_p r_1) j_{\ell_2}(k_q r_2) \delta_{pq}$$

$$= \lim_{\Delta_{\ln k} \rightarrow 0} \Delta_{\ln k} \sum_p \Delta_{\ln k} \sum_q \frac{f(k_p) \delta_{pq}}{\Delta_{\ln k}} j_{\ell_1}(k_p r_1) j_{\ell_2}(k_q r_2), \quad (8)$$

we find that it is a special case of the quadrature integration of the non-Gaussian case Eq. (2) when we take k_1, k_2

as the same array and take the input function $f(k_1, k_2)$ as a diagonal matrix related to the input N -array $f(q)$, i.e., $f(k_1, k_2) = \Delta_{\ln k}^{-1} \text{diag}\{f(q_1), f(q_2), \dots, f(q_{N-1})\}$. Hence, it can be evaluated with the same 2D-FFTLog method in §2.1. Note that this method is only an approximation and requires the discretization. However, its accuracy improves with increasingly finer sampling of k , just as any other numerical integration.

Further speed-up can be achieved by realizing that the 2D discrete Fourier transform of a diagonal matrix is a circulant matrix. Therefore, one can (1D) Fourier transform the N -array $f(q_i)/\Delta_{\ln k}$ to obtain the first row of c_{mn} (which is only an $\mathcal{O}(N \log N)$ algorithm), and then apply $N-1$ cyclic permutations to the first row, to generate the remaining $N-1$ rows. In the context of non-Gaussian covariances, this optimization is negligible, since the total runtime will be dominated by the non-Gaussian computation which scales as $\mathcal{O}(N^2 \log N)$.

2.2 Bin Averaging

Since correlation function measurements are averaged over r or θ bins of finite width, the same bin average should be applied to the covariance. The bin-averaged covariance can be written as

$$\text{Cov}(\bar{r}_i, \bar{r}_j) = \frac{\int_{\bar{r}_{i,\min}}^{\bar{r}_{i,\max}} dr_1 \int_{\bar{r}_{j,\min}}^{\bar{r}_{j,\max}} dr_2 r_1^{D-1} r_2^{D-1} \text{Cov}(r_1, r_2)}{\int_{\bar{r}_{i,\min}}^{\bar{r}_{i,\max}} dr_1 r_1^{D-1} \int_{\bar{r}_{j,\min}}^{\bar{r}_{j,\max}} dr_2 r_2^{D-1}}, \quad (9)$$

where D is the dimension of the statistics (i.e., $D = 2$ for projected statistics, and $D = 3$ for 3D statistics), \bar{r}_i, \bar{r}_j denote the i -th and j -th bins, and the subscripts \min and \max denote the bin edges. Substituting Eq. (5) into Eq. (9) and abbreviating the denominator of Eq. (9) as A , we obtain

$$\begin{aligned} \text{Cov}(\bar{r}_i, \bar{r}_j) &= \frac{\pi}{16AN^2} \sum_{m,n=-N/2}^{N/2} c_{mn} k_0^{-i(\eta_m+\eta_n)} g_{\ell_1}(\nu_1 + i\eta_m) g_{\ell_2}(\nu_2 + i\eta_n) \int_{\bar{r}_{i,\min}}^{\bar{r}_{i,\max}} r_1^{-i\eta_m - \nu_1 + D - 1} dr_1 \int_{\bar{r}_{j,\min}}^{\bar{r}_{j,\max}} r_2^{-i\eta_n - \nu_2 + D - 1} dr_2 \\ &= \frac{\pi}{16AN^2} \sum_{m,n=-N/2}^{N/2} c_{mn} k_0^{-i(\eta_m+\eta_n)} g_{\ell_1}(\nu_1 + i\eta_m) g_{\ell_2}(\nu_2 + i\eta_n) \bar{r}_{i,\min}^{-i\eta_m - \nu_1 + D} \bar{r}_{j,\min}^{-i\eta_n - \nu_2 + D} \\ &\quad \times \frac{[(\bar{r}_{i,\max}/\bar{r}_{i,\min})^{-i\eta_m - \nu_1 + D} - 1]}{D - \nu_1 - i\eta_m} \frac{[(\bar{r}_{j,\max}/\bar{r}_{j,\min})^{-i\eta_n - \nu_2 + D} - 1]}{D - \nu_2 - i\eta_n} \\ &= \frac{\pi \bar{r}_{i,\min}^{D-\nu_1} \bar{r}_{j,\min}^{D-\nu_2}}{16AN^2} \sum_{m,n=-N/2}^{N/2} c_{mn} k_0^{-i(\eta_m+\eta_n)} \bar{r}_{i,\min}^{-i\eta_m} \bar{r}_{j,\min}^{-i\eta_n} g_{\ell_1}(\nu_1 + i\eta_m) g_{\ell_2}(\nu_2 + i\eta_n) s(D - \nu_1 - i\eta_m, \lambda) s(D - \nu_2 - i\eta_n, \lambda), \quad (10) \end{aligned}$$

where we define λ as the logarithmic bin width, i.e., $\bar{r}_{i,\max}/\bar{r}_{i,\min} = e^\lambda$ for every bin, and

$$s(z, \lambda) = \frac{e^{\lambda z} - 1}{z}. \quad (11)$$

$$A = \int_{\bar{r}_{i,\min}}^{\bar{r}_{i,\max}} dr_1 r_1^{D-1} \int_{\bar{r}_{j,\min}}^{\bar{r}_{j,\max}} dr_2 r_2^{D-1} = \bar{r}_{i,\min}^D \bar{r}_{j,\min}^D [s(D, \lambda)]^2. \quad (12)$$

Thus, to accurately compute the bin-averaged covariance, we only need to multiply a few functions s before applying the 2D IFFT, i.e.,

$$\begin{aligned} \text{Cov}(\bar{r}_i, \bar{r}_j) &= \frac{\pi}{16\bar{r}_{i,\min}^{\nu_1} \bar{r}_{j,\min}^{\nu_2}} \text{IFFT2} \left[c_{mn}^*(k_0 r_0)^{i(\eta_m+\eta_n)} \right. \\ &\quad \left. \times g_{\ell_1}(\nu_1 - i\eta_m) g_{\ell_2}(\nu_2 - i\eta_n) \frac{s(D - \nu_1 - i\eta_m, \lambda) s(D - \nu_2 - i\eta_n, \lambda)}{[s(D, \lambda)]^2} \right]. \quad (13) \end{aligned}$$

The above equation works for the covariances of 3D correlation functions. Bin-averaged covariances of projected correlation functions (in the flat sky limit) require a slight modification due to the additional power $r^{1/2}$ from the conversion between the Bessel functions and the spherical Bessel functions (see Eqs. 17 and 18).

Note that starting with a finely sampled k array, IFFT2 will return an equally finely sampled covariance (since we define $\Delta_{\ln r} = \Delta_{\ln k}$). Qualitatively, the numerical accuracy

improves with increasing sampling points given the integration range. Since bin-averaging acts as a smoothing operation, high accuracy can be achieved with less fine sampling compared to the non-bin-averaged case. The actual number of sampling points needed depends on the function to be transformed, the order of Bessel functions and the range and spacing of the r bins. We recommend to test over increasing sampling points until the results converge within the required accuracy. We also recommend to zero-pad the function $f(k_1, k_2)$ to alleviate the ringing effects.

3 APPLICATION TO PROJECTED STATISTICS: 3×2PT COVARIANCE

The 3×2 pt analysis, combining cosmic shear, galaxy-galaxy lensing, and galaxy clustering, has become a standard combination of probes in DES and LSST.

Following the notations in Krause et al. (2017), in the flat sky limit, we write the real space covariance of two an-

gular two-point functions $\Xi, \Theta \in \{w, \gamma_t, \xi_+, \xi_-\}$ as

$$\begin{aligned} & \text{Cov}(\Xi^{ij}(\theta_1), \Theta^{km}(\theta_2)) \\ &= \frac{1}{4\pi^2} \int \frac{d\ell_1}{\ell_1} \int \frac{d\ell_2}{\ell_2} \ell_1^2 \ell_2^2 J_n(\Xi)(\ell_1 \theta_1) J_n(\Theta)(\ell_2 \theta_2) \\ & \quad \times \left[\text{Cov}^G \left(C_{\Xi}^{ij}(\ell_1), C_{\Theta}^{km}(\ell_2) \right) + \text{Cov}^{\text{NG}} \left(C_{\Xi}^{ij}(\ell_1), C_{\Theta}^{km}(\ell_2) \right) \right], \end{aligned} \quad (14)$$

where w is the galaxy angular clustering correlation, γ_t is the galaxy-galaxy lensing two-point correlation, $\xi_{+/-}$ are the cosmic shear two-point correlations. The angular power spectra $C_{\xi_{+/-}} \equiv C^{ee}$, $C_{\gamma_t} \equiv C^{\text{ge}}$, $C_w \equiv C^{\text{gg}}$, denoting the correlations between galaxy densities g and galaxy shapes e , are detailed in §4.1.2. The order of the Bessel function is given by $n = 0$ for ξ_+ and w , $n = 2$ for γ_t , and $n = 4$ for ξ_- . θ_1, θ_2 are angular separations, ℓ_1, ℓ_2 are the angular wave numbers, and i, j, k, m specify the tomography bins. The non-Gaussian covariance Cov^{NG} consists of a connected four-point correlation contribution (e.g., Cooray & Sheth 2002; Takada & Jain 2009) and a super sample contribution (e.g., Krause & Eifler 2017). The Gaussian covariance Cov^G (Hu & Jain 2004) contains a Kronecker delta function $\delta_{\ell_1 \ell_2}$ which reduces the dimension of the integral.

Connection to 2D-FFTLog The integral Eq. (14) can be written in the form of Eq. (2) by realizing that $J_n(z) = \sqrt{2z/\pi} j_{n-1/2}(z)$, i.e., the integral has the form

$$\begin{aligned} & \text{Cov}(\Xi^{ij}(\theta_1), \Theta^{km}(\theta_2)) \\ &= \sqrt{\theta_1 \theta_2} \int \frac{d\ell_1}{\ell_1} \int \frac{d\ell_2}{\ell_2} j_{n(\Xi)-\frac{1}{2}}(\ell_1 \theta_1) j_{n(\Theta)-\frac{1}{2}}(\ell_2 \theta_2) f(\ell_1, \ell_2), \end{aligned} \quad (15)$$

$$\text{Cov}(\bar{\theta}_i, \bar{\theta}_j) = \frac{\pi}{16 \bar{\theta}_{i,\min}^{\nu_1-1/2} \bar{\theta}_{j,\min}^{\nu_2-1/2}} \text{IFFT2} \left[c_{mn}^* (\ell_0 \theta_0)^{i(\eta_m + \eta_n)} g_{n_1-\frac{1}{2}}(\nu_1 - i\eta_m) g_{n_2-\frac{1}{2}}(\nu_2 - i\eta_n) \frac{s(D + \frac{1}{2} - \nu_1 - i\eta_m, \lambda) s(D + \frac{1}{2} - \nu_2 - i\eta_n, \lambda)}{[s(D, \lambda)]^2} \right], \quad (18)$$

where $D = 2$, ℓ_0 is the smallest sampled angular wave number and θ_0 is the smallest sampled angular separation. n_1, n_2 are the orders of (cylindrical) Bessel functions in Eq. (14).

4 VALIDATION FOR FUTURE SURVEY ANALYSES

We implement the 2D-FFTLog algorithm into the covariance module of the COSMOLIKE analysis framework (Eifler et al. 2014; Krause & Eifler 2017). To validate the angular bin-averaged flat sky 3x2pt covariance computed with the 2D-FFTLog algorithm, we also implement an angular bin-averaged flat sky covariance using a brute-force (BF) quadrature integration, and an angular bin-averaged curved sky covariance (detailed in §4.1.4). The curved sky covariance is the most accurate among the three by definition.

We compute the three 3x2pt covariances for a DES Y3-like and an LSST Y1-like survey. Negligible differences are found between the flat sky covariances and the curved

where $f(\ell_1, \ell_2)$ is given by

$$\begin{aligned} f(\ell_1, \ell_2) = & \frac{1}{2\pi^3} \ell_1^{5/2} \ell_2^{5/2} \left[\text{Cov}^G \left(C_{\Xi}^{ij}(\ell_1), C_{\Theta}^{km}(\ell_2) \right) \right. \\ & \left. + \text{Cov}^{\text{NG}} \left(C_{\Xi}^{ij}(\ell_1), C_{\Theta}^{km}(\ell_2) \right) \right] \end{aligned} \quad (16)$$

This integral is now ready for our 2D-FFTLog method.

For better numerical accuracy and stability, we calculate the Gaussian and non-Gaussian parts separately. In addition, the Gaussian part integrand usually contains terms like $[C_{AC}(\ell_1) + N_A][C_{BD}(\ell_2) + N_B]$, where C are angular power spectra of two random fields specified by the subscripts and N are noise terms. The pure noise term $N_A N_B$, if nonzero, is taken out of the integral because the corresponding term is analytically solvable and by doing so, the double Bessel integral is numerically more stable.

Bin Averaging in Flat Sky Limit The covariance is averaged in each angular bin, i.e.,

$$\text{Cov}(\bar{\theta}_i, \bar{\theta}_j) = \frac{\int_{\bar{\theta}_{i,\min}}^{\bar{\theta}_{i,\max}} d\theta_1 \int_{\bar{\theta}_{j,\min}}^{\bar{\theta}_{j,\max}} d\theta_2 \theta_1 \theta_2 \text{Cov}(\theta_1, \theta_2)}{\int_{\bar{\theta}_{i,\min}}^{\bar{\theta}_{i,\max}} d\theta_1 \theta_1 \int_{\bar{\theta}_{j,\min}}^{\bar{\theta}_{j,\max}} d\theta_2 \theta_2}, \quad (17)$$

where $\bar{\theta}_i, \bar{\theta}_j$ are i -th and j -th angular bins, and the subscripts \min and \max denote the lower and upper bin edges. However, we cannot directly apply Eq. (13) with $D = 2$ due to the additional $\sqrt{\theta_1 \theta_2}$ factor in Eq. (15). Following the derivation in §2.2, we obtain the modified bin-averaging result

sky covariances. To confirm that the differences do not impact on the cosmological constraints, we perform simulated 3x2pt likelihood analyses using Monte Carlo Markov Chains (MCMC) with these covariances.

4.1 Analysis Ingredients

4.1.1 Lens and Source Galaxy Sample Distributions

We assume a DES Y3-like survey covering 5000 deg². All other analysis settings are adopted from the DES Y1 analysis (Elvin-Poole et al. 2018; Cawthon et al. 2018). Specifically, we assume a REDMAGIC (Roza et al. 2016) lens sample, split into 5 tomographic bins. The galaxy number density in each bin is [0.0134, 0.0343, 0.0505, 0.0301, 0.0089] per arcmin², and the fiducial linear galaxy bias parameters are set as [1.44, 1.70, 1.70, 2.00, 2.06]. For the source sample, we assume a METACALIBRATION selected sample (Huff & Mandelbaum 2017; Sheldon & Huff 2017; Zuntz et al. 2018), split into 4 bins again similar to the DES Y1 analysis (Hoyle et al. 2018; Troxel et al. 2018). The source galaxy number density

in each bin is [1.496, 1.5189, 1.5949, 0.7949] per arcmin². We also assume shape noise consistent with DES Y1, i.e., $\sigma_\epsilon = 0.279$ per ellipticity component.

For LSST Y1, we generate the redshift distributions of the lens and source galaxies following the DESC Science Requirements Document (DESC SRD, [The LSST Dark Energy Science Collaboration et al. 2018](#)). Our LSST Y1-like survey has a survey area of 12300 deg², and is expected to measure galaxies with an i-band limit of 24.1 mag for the large-scale structure (lens sample) and an i-band depth 25.1 mag for the weak lensing (source sample). For the lens sample, we use a parametric redshift distribution consistent with the DESC SRD, i.e., $dN/dz \propto z^2 \exp[-(z/z_0)^\alpha]$, with $(z_0, \alpha) = (0.26, 0.94)$, normalized by the effective number density $n_{\text{eff}} = 18 \text{ arcmin}^{-2}$. We then split the sample into 5 equally populated tomographic bins (different from the DESC SRD) and convolve each bin with a Gaussian photo- z scatter with $\sigma_z = 0.03(1+z)$. We set the fiducial linear galaxy bias parameter for each bin as $b_i = 1.05/G(\bar{z}^i)$, where \bar{z}^i is the mean redshift of the i -th bin, and $G(z)$ is the linear growth factor. For the source sample, we use the same parametric form but with $(z_0, \alpha) = (0.191, 0.870)$, normalized to $n_{\text{eff}} = 11.2 \text{ arcmin}^{-2}$.¹² We also split the source sample into 5 equally populated tomographic bins and convolve each bin with a Gaussian photo- z uncertainty with $\sigma_z = 0.05(1+z)$. The distributions of the LSST Y1 lens and source tomographic bins are the same as in [Fang et al. \(2019\)](#), and are shown on the left panel of Fig. 4 in [Fang et al. \(2019\)](#). We assume the galaxy shape noise to be $\sigma_\epsilon = 0.26$ per component.

4.1.2 Angular Two-Point Functions

We model the galaxy-galaxy lensing (GGL) and the cosmic shear power spectra using the Limber approximation. Including redshift space distortion (RSD), lensing magnification (Mag), galaxy intrinsic alignment (IA), and following the notation in [Fang et al. \(2019\)](#), the GGL power spectrum between lens bin i and source bin j can be written as

$$C_\ell^{\text{g}^i \text{e}^j} = \frac{2}{2\ell+1} \int_0^\infty dk \tilde{\Delta}^{\text{g}^i}(\chi_\ell) \tilde{\Delta}^{\text{e}^j}(\chi_\ell) P_\delta(k, z(\chi_\ell)). \quad (19)$$

The tomographic cosmic shear power spectrum between the source bin i and j can be written as

$$C_\ell^{\text{e}^i \text{e}^j} = \frac{2}{2\ell+1} \int_0^\infty dk \tilde{\Delta}^{\text{e}^i}(\chi_\ell) \tilde{\Delta}^{\text{e}^j}(\chi_\ell) P_\delta(k, z(\chi_\ell)), \quad (20)$$

where ℓ is the angular wavenumber, k is the wavenumber of the Fourier mode, and $\tilde{\Delta}^{\text{g}}, \tilde{\Delta}^{\text{e}}$ are the modified transfer functions of the galaxy number overdensity δ_{g} and the observed galaxy shape e , respectively, following the definitions in Eqs. (4.3-4.5) and (4.12-4.13) in [Fang et al. \(2019\)](#) (also

¹² These values for the source sample are the updated version from private communication with Rachel Mandelbaum.

see [Chisari et al. 2018](#)), i.e.,

$$\begin{aligned} \tilde{\Delta}^{\text{g}} = & \tilde{\Delta}^{\text{D}}(\chi_\ell) + \frac{3\ell(\ell+1)\Omega_{\text{m}}H_0^2(1+z(\chi_\ell))}{c^2k^2} W^{\text{M}}(z(\chi_\ell)) \\ & + \frac{1+8\ell}{(2\ell+1)^2} \frac{f(z(\chi_\ell))}{b(z(\chi_\ell))} \tilde{\Delta}^{\text{D}}(\chi_\ell) \\ & - \frac{4}{2\ell+3} \sqrt{\frac{2\ell+1}{2\ell+3}} \frac{f(z(\chi_{\ell+1}))}{b(z(\chi_{\ell+1}))} \tilde{\Delta}^{\text{D}}(\chi_{\ell+1}), \end{aligned} \quad (21)$$

$$\begin{aligned} \tilde{\Delta}^{\text{e}} = & \sqrt{\frac{(\ell+2)!}{(\ell-2)!}} \left[\frac{3\Omega_{\text{m}}H_0^2(1+z(\chi_\ell))}{2c^2k^2} W^{\text{L}}(z(\chi_\ell)) \right. \\ & \left. + \frac{n_{\text{src}}(z(\chi_\ell))A_{\text{IA}}(z(\chi_\ell))H(z(\chi_\ell))}{c(\ell+1/2)^2} \right], \end{aligned} \quad (22)$$

where $\tilde{\Delta}^{\text{D}}(\chi_\ell) = \frac{1}{c} m_{\text{lens}}(z(\chi_\ell)) b(z(\chi_\ell)) H(z(\chi_\ell))$, $m_{\text{lens}}(z)$ is the redshift distribution of the lens galaxies, $b(z)$ is the linear galaxy bias parameter, $f(z)$ is the logarithmic growth factor, $H(z)$ is the Hubble parameter, and c is the speed of light. The argument $\chi_\ell = \ell/k$ arises from the Limber approximation. $P_\delta(k, z)$ is the nonlinear matter power spectrum at redshift z . $W^{\text{M}}(z)$ and $W^{\text{L}}(z)$ are the lensing magnification kernel function and the lensing kernel function, defined as

$$W^{\text{M}}(z) = \int_z^\infty dz' n_{\text{lens}}(z') \frac{b_{\text{mag}}(z')}{2} \frac{\chi(z') - \chi(z)}{\chi(z')\chi(z)}, \quad (23)$$

$$W^{\text{L}}(z) = \int_z^\infty dz' n_{\text{src}}(z') \frac{\chi(z') - \chi(z)}{\chi(z')\chi(z)}, \quad (24)$$

where $b_{\text{mag}}(z)$ is the magnification bias parameter encapsulating the linear dependence of the galaxy number density on the convergence κ at a given point on the sky, defined such that the galaxy overdensity δ_{g} is changed by $\Delta\delta_{\text{g}} = b_{\text{mag}}\kappa\delta_{\text{g}}$. $n_{\text{src}}(z)$ is the redshift distribution of the source galaxies. We adopt the ‘‘nonlinear linear alignment model’’ of IA (e.g., [Catelan et al. 2001](#); [Hirata & Seljak 2004](#); [Hirata et al. 2007](#); [Joachimi et al. 2011](#); [Troxel & Ishak 2015](#); [Blazek et al. 2015](#); [Krause et al. 2016](#), but see [Blazek et al. \(2019\)](#) for limitation). $A_{\text{IA}}(z)$ is the (dimensionless) alignment amplitude, defined by

$$A_{\text{IA}} = -\frac{C_{1\rho_{\text{cr}}}\Omega_{\text{m}}}{G(z)} a_{\text{IA}} \left(\frac{1+z}{1+z_0} \right)^\eta, \quad (25)$$

where we use $C_{1\rho_{\text{cr}}} \simeq 0.0134$, a normalization derived from SuperCOSMOS observations ([Hirata & Seljak 2004](#); [Bridle & King 2007](#)), z_0 is an arbitrary pivot value for the power-law scalings of the redshift (with index parameter η), which we take $z_0 = 0.62$ in our analysis, following the DES Year 1 choice in [Troxel et al. \(2018\)](#). We have reduced the number of free parameters by absorbing the luminosity dependence into the free parameter a_{IA} .

We model the galaxy clustering auto power spectra $C_\ell^{\text{g}^i \text{g}^i}$ (superscript i denotes the index of the lens tomographic bin) without the Limber approximation, and adopt the method in §4.1 of [Fang et al. \(2019\)](#).

We compute the linear matter power spectrum using the transfer function from [Eisenstein & Hu \(1998\)](#), and the nonlinear matter power spectrum with HALOFIT ([Smith et al. 2003](#); [Takahashi et al. 2012](#)). We calculate the angular two-point correlation functions for galaxy clustering $w^i(\theta)$, GGL $\gamma_t^{ij}(\theta)$, and cosmic shear $\xi_{+/-}^{ij}(\theta)$, using their relation to an-

gular power spectra on the curved sky:

$$w^i(\theta) = \sum_{\ell} \frac{2\ell+1}{4\pi} P_{\ell}(\cos\theta) C_{\ell}^{\xi^i}, \quad (26)$$

$$\gamma_t^{ij}(\theta) = \sum_{\ell} \frac{2\ell+1}{4\pi\ell(\ell+1)} P_{\ell}^2(\cos\theta) C_{\ell}^{\xi^i \xi^j}, \quad (27)$$

$$\xi_{\pm}^{ij}(\theta) = \sum_{\ell} \frac{2\ell+1}{2\pi\ell^2(\ell+1)^2} [G_{\ell,2}^+(\cos\theta) \pm G_{\ell,2}^-(\cos\theta)] C_{\ell}^{\xi^i \xi^j}, \quad (28)$$

where θ is the angular separation, P_{ℓ} and P_{ℓ}^2 are the Legendre polynomial and the associated Legendre polynomial, $G_{\ell,m}^{+/-}$ are given by Eq. (4.19) of Stebbins (1996).

For DES Y3, we compute all correlation functions in 20 logarithmically spaced angular bins over the range $2.5' < \theta < 250'$, while for LSST Y1, we compute all correlation functions in 26 logarithmically spaced angular bins over $2.5' < \theta < 900'$. For each angular bin $[\theta_{\min}, \theta_{\max}]$, the correlation functions are bin-averaged, i.e., replacing $P_{\ell}(\cos\theta)$, $P_{\ell}^2(\cos\theta)$ and $[G_{\ell,2}^+(\cos\theta) \pm G_{\ell,2}^-(\cos\theta)]$ with their bin-averaged functions $\overline{P_{\ell}}$, $\overline{P_{\ell}^2}$ and $\overline{G_{\ell,2}^+ \pm G_{\ell,2}^-}$ (Friedrich et al., in preparation), defined by Eqs. (5.6-5.8) in Fang et al. (2019). Note that this curved sky bin-averaging reduces to the flat sky bin-averaging when θ is small. Our analysis includes all auto-correlations of the lens bins for the galaxy clustering, all combinations of lens and source bins for the GGL, and all auto- and cross-correlations of the source bins for the cosmic shear. Thus, for DES Y3, the data vector contains 5 sets of $w(\theta)$, 20 sets of $\gamma_t(\theta)$, 10 sets of $\xi_+(\theta)$ and 10 sets of $\xi_-(\theta)$, each of which has 20 angular bins. For LSST Y1, the data vector contains 5 sets of $w(\theta)$, 25 sets of $\gamma_t(\theta)$, 15 sets of $\xi_+(\theta)$ and 15 sets of $\xi_-(\theta)$, each of which has 26 angular bins.

4.1.3 Systematics

We parametrize systematic uncertainties through a set of nuisance parameters closely following the DES Y1 analysis (Krause et al. 2017). We also add the lensing magnification effect to the modeling, and marginalize over its amplitude.

Photometric redshift uncertainties The uncertainty in the redshift distribution of the i -th tomographic bin $n^i(z)$ is modeled by one shift parameter Δ_z for each bin of the lens and the source samples, i.e., $n^i(z) = \hat{n}^i(z - \Delta_z^i)$, where the index i traverses over all the lens and source bins, and \hat{n} is the estimated redshift distribution as described in §4.1.1. There are 9 shift parameters in total for DES Y3 and 10 shift parameters for LSST Y1. We take 0 as their fiducial values to generate the simulated data vector, and marginalize over them in the likelihood analyses. For the DES Y3 lens sample, we choose a Gaussian prior with $\mu = 0, \sigma = [4, 3, 3, 5, 11] \times 10^{-3}$ for each $\Delta_{z,\text{lens}}^i$; for the source sample, we choose a Gaussian prior with $\mu = 0, \sigma = 0.005$ for each $\Delta_{z,\text{source}}^i$. For LSST Y1, we choose a Gaussian prior with $\mu = 0, \sigma = 0.005(1 + \bar{z}^i)$ for each $\Delta_{z,\text{lens}}^i$, and a Gaussian prior with $\mu = 0, \sigma = 0.002(1 + \bar{z}^i)$ for each $\Delta_{z,\text{source}}^i$, consistent with the requirements given in §5.1 and 5.2 of the DESC SRD.

Galaxy bias We assume a linear bias model and use one parameter for each lens bin. There are 4 parameters in total

for DES Y3, and 5 for LSST Y1, whose fiducial values are described in §4.1.1 for generating the simulated data vector. In the likelihood analysis, they will be marginalized over with conservative flat priors [0.8, 3].

Lensing magnification bias We parameterize the lensing magnification effect through one parameter for each lens bin b_{mag}^i (see §4.1.2 for modeling details). For magnitude limited samples, magnification due to lensing by line-of-sight structure can affect the number density of galaxies with observed magnitudes exceeding the magnitude cut (e.g., Verner Villumsen 1995; Moessner & Jain 1998; Loverde et al. 2008). For LSST Y1, we assume the lens samples are magnitude limited, and estimate $b_{\text{mag}}^i = (-0.898, -0.659, -0.403, -0.0704, 0.416)$ for the 5 lens bins as in Fang et al. (2019), which is based on the fitting formula in Joachimi & Bridle (2010) and r -band limit given by the DESC SRD. For DES Y3 lens sample, we adopt the DES Year 6 b_{mag} values, $b_{\text{mag}}^i = (-0.102, -0.102, -0.102, 1.06, 1.06)$, that we estimate in Fang et al. (2019), which is based on the Schechter luminosity function (Schechter 1976) and the luminosity cuts $L/L_* > (0.5, 0.5, 0.5, 1.0, 1.0)$ for bins from low to high redshifts, respectively. L_* is the characteristic galaxy luminosity where the power-law form in the Schechter luminosity function cuts off. The 5 nuisance parameters b_{mag}^i are marginalized over conservative flat priors [-3,3] in the likelihood analysis.

Multiplicative shear calibration We use one shear calibration uncertainty parameter m^i per source bin (4 in total for DES Y3, and 5 for LSST Y1), acting on the cosmic shear and GGL correlation functions such that

$$\xi_{+/-}^{ij}(\theta) \rightarrow (1 + m^i)(1 + m^j)\xi_{+/-}^{ij}(\theta), \quad \gamma_t^{ij}(\theta) \rightarrow (1 + m^j)\gamma_t^{ij}(\theta). \quad (29)$$

The m^i are marginalized over independently with Gaussian priors ($\mu = 0, \sigma = 0.005$).

IA We use the nonlinear linear alignment (NLA) model and parameterize it with two parameters a_{IA} and η (see §4.1.2 for modeling details). Their fiducial values are $a_{\text{IA}} = 0.5$ and $\eta = 0$, and they are both marginalized over independently with conservative flat priors [-5, 5].

4.1.4 Covariances

The computation of the bin-averaged flat sky real space covariances is introduced in §3, where the ‘‘flat sky’’ approximation is applied to both the bin-averaging step and the transform from Fourier to real space covariance. For comparison, we also compute the covariances of bin-averaged correlation functions on the curved sky (without the flat sky approximation in either step), i.e., for two angular two-point functions, $\Xi, \Theta \in \{w, \gamma_t, \xi_+, \xi_-\}$

$$\text{Cov}(\Xi^{ij}(\theta), \Theta^{km}(\theta')) = \sum_{\ell} \overline{P_{\ell}^{\Xi}} \sum_{\ell'} \overline{P_{\ell'}^{\Theta}} \text{Cov}(C_{\Xi}^{ij}(\ell), C_{\Theta}^{km}(\ell')), \quad (30)$$

where $C_{\xi_+} = C_{\xi_-} = C^{ee}$, $C_{\gamma_t} = C^{\xi\xi}$, and $C_w = C^{\xi\xi}$ in our previous notation, and i, j, k, m are the tomographic bin indices.

The bin-averaged weight functions are defined as (Friedrich et al., in preparation)

$$\begin{aligned} \overline{P}_\ell^w &= \frac{2\ell+1}{4\pi} \overline{P}_\ell, & \overline{P}_\ell^{\gamma'} &= \frac{2\ell+1}{4\pi\ell(\ell+1)} \overline{P}_\ell^2, \\ \overline{P}_\ell^{\xi_\pm} &= \frac{2\ell+1}{2\pi\ell^2(\ell+1)^2} \overline{G_{\ell,2}^+ \pm G_{\ell,2}^-}. \end{aligned} \quad (31)$$

In our implementation, we evaluate Eq. (30) up to $\ell_{\max} = 50000$.

4.1.5 Angular Scale Cuts

Survey analyses define a set of angular scale cuts to prevent nonlinear modeling limitations and baryonic feedback processes from biasing the cosmology results. For LSST Y1, we choose a scale cut $k_{\max} = 0.3h/\text{Mpc}$ as in the DESC SRD, which roughly corresponds to a comoving scale $R_{\min} = 2\pi/k_{\max} = 21 \text{ Mpc}/h$. For the galaxy clustering, we define the angular scale cut θ_{\min}^i for lens tomographic bin i as $\theta_{\min}^i = R_{\min}/\chi(\bar{z}^i)$, where \bar{z}^i is the mean redshift of galaxies in tomographic bin i . For the lens sample, θ_{\min}^i are [80.88', 54.19', 42.85', 35.43', 29.73']. The scale cuts for γ_t^{ij} are the same as θ_{\min}^i . For the cosmic shear, we use cuts $\ell < \ell_{\max} = 3000$ as defined in the DESC SRD, and translate it into the angular cuts for $\xi_{+/-}$ with the first zeros of their corresponding Bessel functions $J_{0/4}$ (in the flat sky-limit transform), i.e., $\theta_{\min}^{\xi_+} = 2.4048/\ell_{\max} = 2.756'$, and $\theta_{\min}^{\xi_-} = 7.5883/\ell_{\max} = 8.696'$.

For DES Y3, we adopt $R_{\min} = 8 \text{ Mpc}/h$ for the galaxy clustering, and $R_{\min} = 12 \text{ Mpc}/h$ for the GGL, same as DES Y1 analysis choice (Krause et al. 2017). For cosmic shear, we adopt scale cuts same as those used in DES Y1 cosmic shear analysis (Troxel et al. 2018).

4.2 Covariance Comparison

We implement three versions of the 3x2pt angular bin-averaged covariances: (1) the flat sky covariance using the 2D-FFTLog algorithm, (2) the flat sky covariance using a BF quadrature integration, and (3) the curved sky covariance introduced in §4.1.4.

We first compare these covariances at high level (e.g., eigenvalues and singular values, as well as their signal-to-noise ratios in Fig. 2) in §4.2.1. Then, we estimate the impact of the numerical artifacts in the covariances on the inferred goodness of fit (χ^2) in §4.2.2. Finally in §4.2.3, we test the impact on the inferred means and uncertainties of the cosmological parameters using simulated likelihood analyses.

4.2.1 Elements, Eigenvalues and Singular Values

We provide several high level comparisons of the three versions of 3x2pt angular bin-averaged covariances in terms of their elements, eigenvalues and singular values.

For a visual element-wise comparison, Fig. 1 shows the 900x900 DES Y3 3x2pt real space flat sky correlation matrices $C_{ij}/\sqrt{C_{ii}C_{jj}}$ from FFT and BF methods, where no obvious difference is detectable by eye.

We then compute the eigenvalues of the three DES Y3 covariances and the three LSST Y1 covariances, and further

compute the signal-to-noise ratio (SNR) of each eigenvalue. The total SNR is defined as $\text{SNR}^2 = \mathbf{D}^T \mathbf{C}^{-1} \mathbf{D}$. Since \mathbf{C} is a real symmetric matrix, the eigendecomposition of \mathbf{C} leads to

$$\mathbf{C} = \mathbf{V} \mathbf{\Lambda} \mathbf{V}^T, \quad (32)$$

where $\mathbf{\Lambda}$ is the diagonal matrix of all the eigenvalues λ_i of \mathbf{C} sorted in descending order, and \mathbf{V} is an orthogonal matrix ($\mathbf{V}^{-1} = \mathbf{V}^T$) whose columns are the eigenvectors of \mathbf{C} . Thus, we have

$$\text{SNR}^2 = (\mathbf{V}^T \mathbf{D})^T \mathbf{\Lambda}^{-1} (\mathbf{V}^T \mathbf{D}) = \sum_i \frac{(\mathbf{V}^T \mathbf{D})_i^2}{\lambda_i} = \sum_i \text{SNR}_i^2, \quad (33)$$

where we have defined the SNR of the i -th eigenvalue λ_i in the last equality.

As the flat sky BF LSST Y1 covariance suffers from numerical instabilities with 1 negative eigenvalue, we do not include it in further analyses. Instead, we perform the singular value (SV) decomposition of LSST Y1 covariances, and compute the SNR of each SV. We decompose \mathbf{C} as $\mathbf{C} = \mathbf{U} \mathbf{\Sigma} \mathbf{V}^T$, where \mathbf{U}, \mathbf{V} are both orthogonal, and $\mathbf{\Sigma}$ is a diagonal matrix of all the SVs s_i sorted in descending order. Similar to the eigendecomposition, we have

$$\text{SNR}^2 = (\mathbf{V}^T \mathbf{D})^T \mathbf{\Sigma}^{-1} (\mathbf{U}^T \mathbf{D}) = \sum_i \frac{(\mathbf{U}^T \mathbf{D})_i (\mathbf{V}^T \mathbf{D})_i}{s_i} = \sum_i \text{SNR}_i^2, \quad (34)$$

where we define the SNR for the i -th SV s_i in the last equality.

Fig. 2 shows a comparison of the eigenvalues and SVs of the flat and curved sky covariances. We sort the SNRs of the 900 eigenvalues of the DES Y3 covariances and the 1560 SVs of the LSST Y1 covariances, and then compare the eigenvalues/SVs of flat sky covariances to those of the curved sky covariances. For each survey, the eigenvalues/SVs show few-percent level agreement, and we only show the 100 eigenvalues/200 SVs of the highest SNRs. Overall, the flat sky FFT covariances show better agreement with the curved sky covariance, especially for those eigenvalues/SVs with high SNRs. This may attribute to lower numerical accuracy of the BF calculations, and may result in the negative eigenvalue of the LSST Y1 flat sky BF covariance.

4.2.2 Shifts in χ^2

An inaccurate covariance matrix affects the inferred goodness of fit. The goodness of fit may be quantified by χ^2 in the data vector space, defined as $\chi^2 = (\mathbf{D} - \mathbf{M}(\mathbf{p}))^T \mathbf{C}^{-1} (\mathbf{D} - \mathbf{M}(\mathbf{p}))$, where \mathbf{D} is the 3x2pt data vector, $\mathbf{M}(\mathbf{p})$ is the model vector evaluated with cosmological and nuisance parameters \mathbf{p} , and \mathbf{C} is the covariance matrix.

We assume that the curved sky covariance is the true covariance \mathbf{C}_0 , and that $\mathbf{x} = \mathbf{D} - \mathbf{M}(\mathbf{p})$ follows a Gaussian distribution, $\mathbf{x} \sim N(0, \mathbf{C}_0)$. Using a ‘‘false’’ covariance \mathbf{C}_1 will result in a shift in χ^2 , i.e., $\Delta\chi^2 = \mathbf{x}^T (\mathbf{C}_1^{-1} - \mathbf{C}_0^{-1}) \mathbf{x}$. Both $\mathbf{x}^T \mathbf{C}_1^{-1} \mathbf{x}$ and $\mathbf{x}^T \mathbf{C}_0^{-1} \mathbf{x}$ are quadratic forms. We compute the expectation value and the variance of $\Delta\chi^2$ per degree of free-

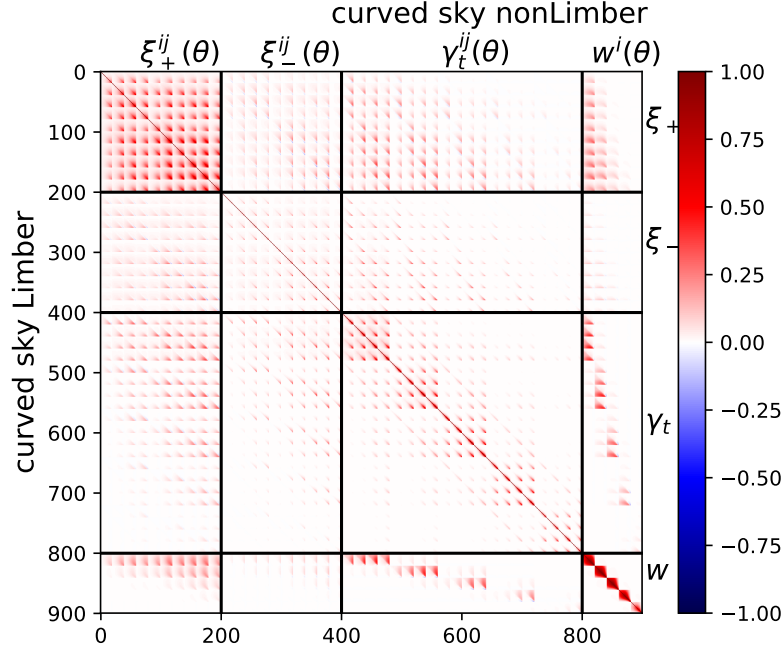


Figure 1. DES Y3 3x2pt real space flat sky correlation matrices from our FFT method (lower triangle) and the brute-force (BF) quadrature integration (upper triangle). The matrices are 900× 900, and the blocks of covariances between different probes are annotated.

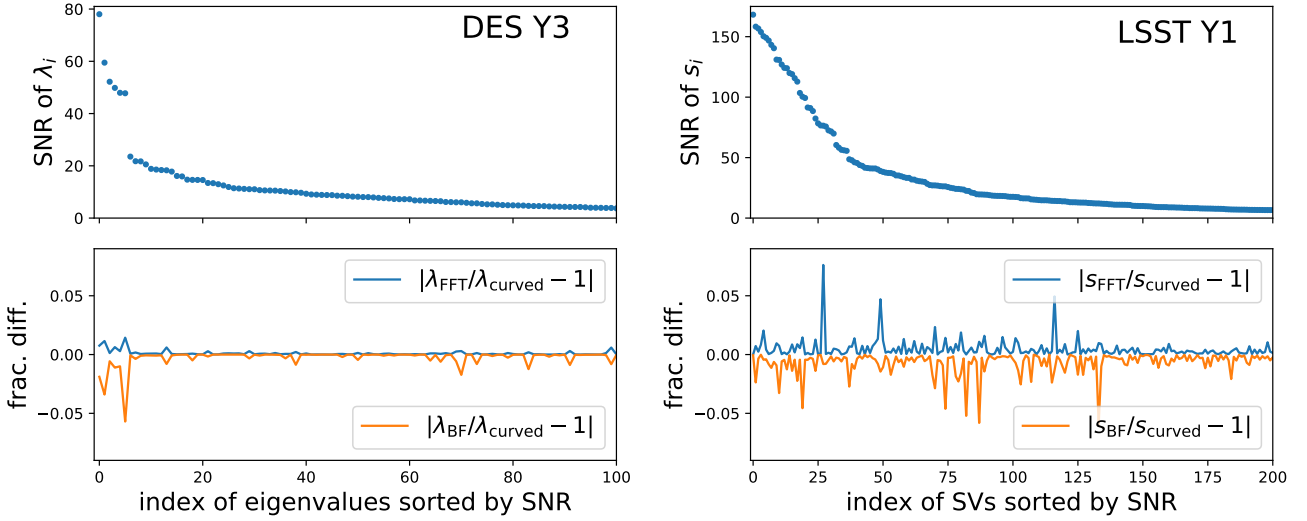


Figure 2. The SNRs of eigenvalues of the DES Y3 curved sky covariance (upper left) and the SNRs of SVs of the LSST Y1 curved sky covariance (upper right), sorted by magnitude. The eigenvalues and SVs are also compared to the flat sky FFT and BF covariances, respectively (lower left and right). For each survey, the flat sky eigenvalues and SVs match the curved sky eigenvalues and SVs within a few percent. We only show the 100 (out of 900) eigenvalues of the highest SNRs for DES Y3, and 200 (out of 1560) SVs for LSST Y1.

dom (d.o.f.),

$$E[\Delta\chi^2/N_D] = \text{tr}(\mathbf{C}_1^{-1}\mathbf{C}_0)/N_D - 1, \quad (35)$$

$$\text{Var}[\Delta\chi^2/N_D] = [2N_D + 4\text{tr}(\mathbf{C}_1^{-1}\mathbf{C}_0\mathbf{C}_1^{-1}\mathbf{C}_0) - 4\text{tr}(\mathbf{C}_1^{-1}\mathbf{C}_0)]/N_D^2, \quad (36)$$

where N_D is the dimension of the data vector (900 for DES Y3 and 1560 for LSST Y1).

Table 1 shows the means and standard deviations of $\Delta\chi^2$

per d.o.f. if the flat sky FFT or BF covariances are used for DES Y3 and LSST Y1, respectively. This χ^2 shift is the χ^2 difference due to the change of covariance matrix only, and does not account for the possible shift in the best-fit values of parameters, which can happen when data vectors are fitted with inaccurate covariances. Given the insignificance of these χ^2 shifts, there is reason to believe that the impact of using the flat sky covariances for DES Y3 and LSST Y1 on

the goodness of fit is negligible. However, we note that the corresponding χ^2 shifts for fitting noisy data vectors can be larger and needs to be checked on a case by case basis.

4.2.3 Simulated Likelihood Analysis

An inaccurate covariance ultimately affects the inferred cosmological parameter constraints. We investigate this impact by performing simulated likelihood analyses.

We generate the simulated 3x2pt data vector \mathbf{D} by computing the model vector at the fiducial parameter values and in our fiducial cosmology, i.e., the standard Λ CDM with massless neutrinos, with non-Limber modeling of w and γ_t (see §4.2 of Fang et al. 2019, for modeling details of γ_t), and Limber modeling of $\xi_{+/-}$. Throughout our analyses, we use the EMCEE sampler (Foreman-Mackey et al. 2013). The fiducial values and priors of the parameters (30 parameters are sampled for DES Y3, and 32 for LSST Y1) are summarized in Table 2. We focus on the cosmological parameter subspace $(\Omega_m, \sigma_8, n_s)$, since galaxy clustering and weak lensing are most powerful in constraining Ω_m and σ_8 , while n_s is a good indicator of whether the model has sufficiently corrected the parameter biases due to the Limber approximation (Fang et al. 2019).

The left panel of Fig. 3 shows the constraints on the 3 cosmological parameters from simulated DES Y3 analyses with the three different covariances. They all recover the fiducial values of the cosmological parameters with nearly identical constraints. The right panel shows a comparison of the cosmological constraints from simulated LSST Y1 analyses with the two different covariances, and we again find good agreement of the inferred best fit parameters and their uncertainties. We conclude that the 2D-FFTLLog algorithm is sufficiently accurate, and that using the flat sky limit of the 3x2pt covariance up to 900 arcmins angular separation will not bias the cosmological parameters $(\Omega_m, \sigma_8, n_s)$ for an LSST Y1-like 3x2pt analysis.

5 DISCUSSION AND SUMMARY

Statistical inference of cosmological parameters for future surveys require precise covariance matrices. The covariance matrices can be estimated from data or an ensemble of simulations, or calculated analytically. Computing covariances analytically is much faster and less noisy. However, the transform of covariance matrices from Fourier space to real space involves integrals with two Bessel integrals (for 3D statistics or projected statistics at flat sky limit), which are numerically unstable due to the oscillatory nature of the integrand. These numerical issues are more severe for large angular separation of the correlation functions and for lower noise (i.e., for higher number density of galaxies or lower shape noise of weak lensing shear measurements), leading to longer computation time. The issue is exacerbated for higher dimensional covariance matrices, as the computation time grows quadratically with the dimension.

We present a 2D-FFTLLog algorithm to accurately and efficiently compute the real space bin-averaged Gaussian and non-Gaussian covariances (§2). We apply the algorithm to the covariances of angular correlation functions of galaxy clustering, galaxy-galaxy lensing, and cosmic shear (§3), and

validate our method for DES Y3-like and LSST Y1-like surveys (§4). For both surveys, we compare the flat sky FFT covariance to the exact, but computationally slow, curved sky transformation, the ‘‘curved sky covariance’’, and find that the flat sky FFT covariance is sufficiently accurate and does not bias cosmological parameters, even at LSST Y1 precision.

The 2D-FFTLLog algorithm can also be applied to other real space covariances of projected statistics, such as 5x2pt, 6x2pt (joint analyses of 3x2pt and CMB lensing, Schaap et al. 2017; Baxter et al. 2019; Abbott et al. 2019), and cluster clustering and lensing, where the method in §3 is directly applicable, as well as covariances of 3D statistics, such as multipoles of galaxy 3D correlation functions (e.g., Grieb et al. 2016), where the method in §2 is directly applicable.

The 2D-FFTLLog code, written in both python and C, is publicly available at <https://github.com/xfangcosmo/2DFFTLLog>. The C code is incorporated into COSMOLIKE (Krause & Eifler 2017). We release an improved version of the real-space 3x2pt covariance code COSMOCOV that we have built for this paper at <https://github.com/CosmoLike/CosmoCov>.

ACKNOWLEDGMENTS

We thank Oliver Friedrich, Niall MacCrann, Jonathan Blazek, Marko Simonović, Vivian Miranda for helpful discussions and comments. We thank Oliver Friedrich and Stella Seitz for their distributed notes on bin-averaging and curved sky covariances, and Rachel Mandelbaum for the updated LSST Y1 source sample distribution. We also thank Shivam Pandey and Anna Porredon for testing COSMOCOV. XF, TE are supported by NASA ROSES ATP 16-ATP16-0084 grant. TE is supported by Department of Energy grant DE-SC0020215. EK is supported by Department of Energy grant DE-SC0020247. Calculations in this paper use High Performance Computing (HPC) resources supported by the University of Arizona TRIF, UITS, and RDI and maintained by the UA Research Technologies department.

REFERENCES

- Abbott T. M. C., et al., 2018, *Phys. Rev. D*, **98**, 043526
 Abbott T. M. C., et al., 2019, *Phys. Rev. D*, **100**, 023541
 Abramowitz M., Stegun I. A., 1972, Handbook of Mathematical Functions
 Akeret J., Refregier A., Amara A., Seehars S., Hasner C., 2015, *J. Cosmology Astropart. Phys.*, **2015**, 043
 Assasi V., Simonović M., Zaldarriaga M., 2017, *J. Cosmology Astropart. Phys.*, **11**, 054
 Baxter E. J., et al., 2019, *Phys. Rev. D*, **99**, 023508
 Blazek J., Vlah Z., Seljak U., 2015, *J. Cosmology Astropart. Phys.*, **2015**, 015
 Blazek J., MacCrann N., Troxel M. A., Fang X., 2019, *Phys. Rev. D*, **100**, 103506
 Bridle S., King L., 2007, *New Journal of Physics*, **9**, 444
 Catelan P., Kamionkowski M., Blandford R. D., 2001, *MNRAS*, **320**, L7
 Cawthon R., et al., 2018, *MNRAS*, **481**, 2427
 Chisari N. E., et al., 2018, arXiv e-prints, p. arXiv:1812.05995
 Cooray A., Sheth R., 2002, *Phys. Rep.*, **372**, 1
 Dodelson S., Schneider M. D., 2013, *Phys. Rev. D*, **88**, 063537

Surveys	d.o.f.	$\Delta\chi^2$ per d.o.f.	
		FFT vs curved	BF vs curved
DES Y3 no scale cuts	900	0.00074 ± 0.00041	0.00174 ± 0.00058
DES Y3 with scale cuts	447	0.00160 ± 0.00075	0.00313 ± 0.00101
LSST Y1 no scale cuts	1560	0.00159 ± 0.00154	–
LSST Y1 with scale cuts	1059	0.00359 ± 0.00208	–

Table 1. The χ^2 shifts per d.o.f. of using the flat sky FFT/BF covariances for DES Y3-like and LSST Y1-like surveys, assuming that the curved sky covariances are true. Both surveys with and without scale cuts are considered. The flat sky BF covariance of LSST Y1 is not included as it is not invertible in our implementation. The insignificance of these χ^2 shifts indicates negligible impact of using the flat sky covariances for DES Y3 and LSST Y1 on the goodness of fit.

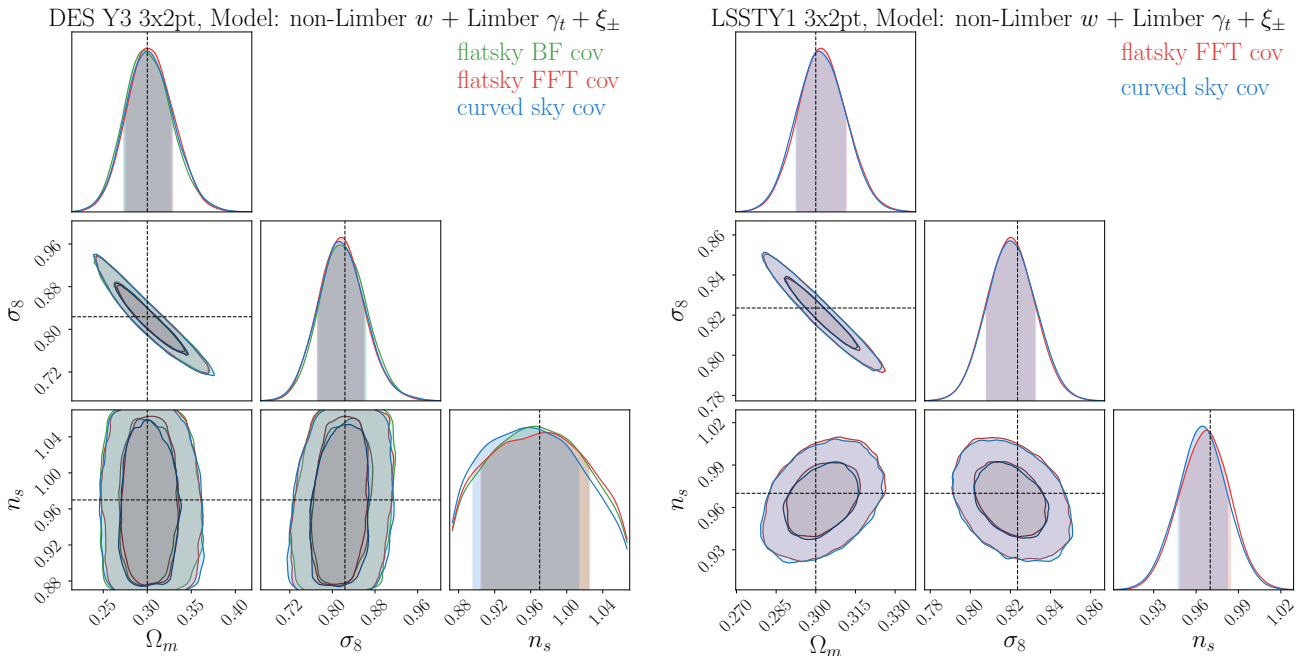


Figure 3. The 1σ and 2σ contours of fitting the simulated 2×2 pt data vector with the model, using bin-averaged flat sky covariances and the curved sky covariances for DES Y3 (left) and LSST Y1 (right). For DES Y3, we have two versions of flat sky covariances from the brute-force (BF) quadrature integration and our 2D-FFTLLog algorithm. For LSST Y1, we only compare the FFT result to the curved sky result.

Eifler T., Krause E., Schneider P., Honscheid K., 2014, *MNRAS*, **440**, 1379
 Eisenstein D. J., Hu W., 1998, *ApJ*, **496**, 605
 Elvin-Poole J., et al., 2018, *Phys. Rev. D*, **98**, 042006
 Fang X., Blazek J. A., McEwen J. E., Hirata C. M., 2017, *J. Cosmology Astropart. Phys.*, **2**, 030
 Fang X., Krause E., Eifler T., MacCrann N., 2019, arXiv e-prints, p. arXiv:1911.11947
 Foreman-Mackey D., Hogg D. W., Lang D., Goodman J., 2013, *PASP*, **125**, 306
 Friedrich O., Eifler T., 2018, *MNRAS*, **473**, 4150
 Grasshorn Gebhardt H. S., Jeong D., 2018, *Phys. Rev. D*, **97**, 023504
 Grieb J. N., Sánchez A. G., Salazar-Albornoz S., Dalla Vecchia C., 2016, *MNRAS*, **457**, 1577
 Hamana T., et al., 2019, arXiv e-prints, p. arXiv:1906.06041
 Hamilton A. J. S., 2000, *MNRAS*, **312**, 257
 Hartlap J., Simon P., Schneider P., 2007, *A&A*, **464**, 399
 Hartlap J., Schrabback T., Simon P., Schneider P., 2009, *A&A*, **504**, 689
 Hildebrandt H., et al., 2017, *MNRAS*, **465**, 1454

Hirata C. M., Seljak U., 2004, *Phys. Rev. D*, **70**, 063526
 Hirata C. M., Mandelbaum R., Ishak M., Seljak U., Nichol R., Pimbblet K. A., Ross N. P., Wake D., 2007, *MNRAS*, **381**, 1197
 Hoyle B., et al., 2018, *MNRAS*, **478**, 592
 Hu W., Jain B., 2004, *Phys. Rev. D*, **70**, 043009
 Huff E., Mandelbaum R., 2017, arXiv e-prints, p. arXiv:1702.02600
 Joachimi B., 2017, *MNRAS*, **466**, L83
 Joachimi B., Bridle S. L., 2010, *A&A*, **523**, A1
 Joachimi B., Mandelbaum R., Abdalla F. B., Bridle S. L., 2011, *A&A*, **527**, A26
 Krause E., Eifler T., 2017, *MNRAS*, **470**, 2100
 Krause E., Eifler T., Blazek J., 2016, *MNRAS*, **456**, 207
 Krause E., et al., 2017, arXiv e-prints, p. arXiv:1706.09359
 Lee H., Dvorkin C., 2020, arXiv e-prints, p. arXiv:2001.00584
 Li Y., Singh S., Yu B., Feng Y., Seljak U., 2019, *Journal of Cosmology and Astro-Particle Physics*, **2019**, 016
 Lin C.-H., Harnois-Déraps J., Eifler T., Pospisil T., Mandelbaum R., Lee A. B., Singh S., 2019, arXiv e-prints, p. arXiv:1905.03779

Parameters	Fiducial	Prior
Survey		
Ω_{survey}	DES 5000 deg ² ; LSST 12300 deg ²	fixed
σ_e per component	DES 0.279; LSST 0.26	fixed
Cosmology		
Ω_m	0.3	flat [0.1, 0.9]
σ_8	0.82355	flat [0.4, 1.2]
n_s	0.97	flat [0.87, 1.07]
Ω_b	0.048	flat [0.03, 0.07]
h_0	0.69	flat [0.55, 0.91]
w_0	-1	fixed
w_a	0	fixed
Σm_ν	0	fixed
Galaxy Bias		
b^i	DES [1.44, 1.70, 1.70, 2.00, 2.06]; LSST [1.24, 1.36, 1.47, 1.60, 1.76]	flat [0.8, 3]
Magnification Bias		
b_{mag}^i	DES [-0.102, -0.102, -0.102, 1.06, 1.06]; LSST [-0.898, -0.659, -0.403, -0.0704, 0.416]	flat [-3, 3]
Lens/Source Photo-z		
$\Delta_{z,\text{lens}}^i$	0	LSST Gauss (0, 0.005(1 + \bar{z}_{lens}^i)); DES Gauss (0, [4, 3, 3, 5, 11] × 10 ⁻³)
$\Delta_{z,\text{source}}^i$	0	LSST Gauss (0, 0.002(1 + \bar{z}_{src}^i)); DES Gauss (0, 0.005(1 + \bar{z}_{src}^i))
Shear Calibration		
m^i	0	Gauss (0, 0.005)
IA		
a_{IA}	0.5	flat [-5, 5]
η	0	flat [-5, 5]

Table 2. A list of the parameters characterizing the surveys, cosmology and systematics. The entries are separated by a semi-colon if they are different for DES Y3 and LSST Y1; otherwise, we only write out the shared entry. The fiducial values are used for generating the simulated data vector, and the priors are used in the sampling. Flat priors are described by [minimum, maximum], and Gaussian priors are described by Gauss (μ, σ).

Loverde M., Hui L., Gaztañaga E., 2008, *Phys. Rev. D*, **77**, 023512
McEwen J. E., Fang X., Hirata C. M., Blazek J. A., 2016, *J. Cosmology Astropart. Phys.*, **9**, 015
Moessner R., Jain B., 1998, *MNRAS*, **294**, L18
Peel A., Lin C.-A., Lanusse F., Leonard A., Starck J.-L., Kilbinger M., 2017, *A&A*, **599**, A79
Rozo E., et al., 2016, *MNRAS*, **461**, 1431
Sato M., Ichiki K., Takeuchi T. T., 2010, *Phys. Rev. Lett.*, **105**, 251301
Schaan E., Krause E., Eifler T., Doré O., Miyatake H., Rhodes J., Spergel D. N., 2017, *Phys. Rev. D*, **95**, 123512
Schechter P., 1976, *ApJ*, **203**, 297
Schmittfull M., Vlah Z., 2016, *Phys. Rev. D*, **94**, 103530
Schmittfull M., Vlah Z., McDonald P., 2016, *Phys. Rev. D*, **93**, 103528
Schöneberg N., Simonović M., Lesgourgues J., Zaldarriaga M., 2018, preprint, ([arXiv:1807.09540](https://arxiv.org/abs/1807.09540))
Sellentin E., Heavens A. F., 2016, *MNRAS*, **456**, L132
Sellentin E., Heavens A. F., 2017, *MNRAS*, **464**, 4658
Sheldon E. S., Huff E. M., 2017, *ApJ*, **841**, 24
Simonović M., Baldauf T., Zaldarriaga M., Carrasco J. J., Kollmeier J. A., 2018, *J. Cosmology Astropart. Phys.*, **4**, 030

Singh S., Mandelbaum R., Seljak U., Slosar A., Vazquez Gonzalez J., 2017, *MNRAS*, **471**, 3827
Slepian Z., 2018, arXiv e-prints, [p. arXiv:1812.02728](https://arxiv.org/abs/1812.02728)
Slepian Z., Li Y., Schmittfull M., Vlah Z., 2019, arXiv e-prints, [p. arXiv:1912.00065](https://arxiv.org/abs/1912.00065)
Smith R. E., et al., 2003, *MNRAS*, **341**, 1311
Stebbins A., 1996, arXiv e-prints, [pp astro-ph/9609149](https://arxiv.org/abs/astro-ph/9609149)
Takada M., Jain B., 2009, *MNRAS*, **395**, 2065
Takahashi R., Sato M., Nishimichi T., Taruya A., Oguri M., 2012, *ApJ*, **761**, 152
Taylor A., Joachimi B., 2014, *MNRAS*, **442**, 2728
Taylor A., Joachimi B., Kitching T., 2013, *MNRAS*, **432**, 1928
The LSST Dark Energy Science Collaboration et al., 2018, arXiv e-prints, [p. arXiv:1809.01669](https://arxiv.org/abs/1809.01669)
Troxel M. A., Ishak M., 2015, *Phys. Rep.*, **558**, 1
Troxel M. A., et al., 2018, *Phys. Rev. D*, **98**, 043528
Verner Villumsen J., 1995, arXiv e-prints, [pp astro-ph/9512001](https://arxiv.org/abs/astro-ph/9512001)
Zuntz J., et al., 2018, *MNRAS*, **481**, 1149

This paper has been typeset from a $\text{\TeX}/\text{\LaTeX}$ file prepared by the author.